Research Square

Preprints are preliminary reports that have not undergone peer review.
They should not be considered conclusive, used to inform clinical practice,
or referenced by the media as validated information.

Balancing Power Harvesting and Data Reception in Inverted Perovskite SLIPT Receivers

Tariq Sajjad

sajjadt@lsbu.ac.uk

London South Bank University https://orcid.org/0000-0001-6932-8686

Himal Muwanwella

London South Bank University

Matthew Anderson

University of Cambridge

Antonio Riquelme

Université Grenoble Alpes

Bahattin Bademci

London South Bank University

Huiming Luo

University College London

Siming Huang

University College London

Jonathon Harwell

University of Glasgow

John Buckeridge

London South Bank University

Steven Dunn

London South Bank University

Harald Haas

University of Cambridge

Mojtaba Abdi-Jalebi

University College London https://orcid.org/0000-0002-9430-6371

Iman Tavakkolnia

University of Cambridge https://orcid.org/0000-0003-4736-1949

Article

Keywords: SLIPT, perovskite photovoltaics, visible-light communication, RC-limited bandwidth, impedance spectroscopy, maximum power point operation

Posted Date: March 16th, 2026

DOI: https://doi.org/10.21203/rs.3.rs-8888531/v1

License: This work is licensed under a Creative Commons Attribution 4.0 International License.
Read Full License

Additional Declarations: There is no conflict of interest

Abstract

Simultaneous light and information-power transfer (SLIPT) offer a route to self-powered optical access networks, yet solar cell-based receivers typically face a fundamental trade-off between efficient power harvesting and high-speed data reception. Here we demonstrate inverted perovskite SLIPT receivers that sustain high-speed visible-light communication while operating directly at the electrical maximum power point. By tailoring the hole-transport layer and its interface with the perovskite absorber, we independently tune recombination dynamics and the device RC response, enabling data transmission close to optimal photovoltaic bias. Interface optimisation suppresses parasitic capacitance and contact resistance while preserving a high open-circuit voltage, thereby maintaining strong power-conversion efficiency alongside MHz-scale bandwidths (-3dB bandwidth of ~ 4.5 MHz). In a proof-of-concept SLIPT link, the optimised devices deliver stable data transmission (> 40 Mbps) while harvesting a large fraction of the maximum available electrical power (~ 500 μW), placing them among the fastest perovskite-SLIPT devices reported to date. These results establish interface-engineered inverted perovskites as a viable platform for power-efficient, high-speed SLIPT and provide general design rules for concurrent optical energy harvesting and data reception.

1. Introduction

Metal-halide perovskites (MHP) have rapidly emerged as leading photovoltaic materials, with certified power conversion efficiencies approaching 27%[1]. Beyond solar cells, their strong visible-light absorption, tuneable bandgaps[2], long carrier-diffusion lengths[3], and remarkable defect tolerance [4, 5] have enabled a wide range of optoelectronic devices, including high-performance photodetectors. Perovskite photodetectors (PDs) have demonstrated sub-microsecond response times, MHz-scale bandwidths, and operation across broad spectral ranges[6–8], highlighting their potential for optical communication and sensing.

Despite this versatility, perovskite photodetectors and solar cells are almost universally operated in fundamentally different regimes. High-speed optical detection is typically achieved near short-circuit (SC) conditions, where strong photocurrent dynamics and minimal junction capacitance maximise bandwidth[9]. In contrast, efficient energy harvesting requires operation at the maximum power point (MPP), where the internal electric field is reduced and charge accumulation and recombination dynamics differ markedly[10]. As a result, the photovoltaic functionality of perovskite absorbers remains largely unused in optical communication systems, limiting their applicability for self-sustaining technologies such as distributed sensors, Internet-of-Things nodes, and indoor wireless networks.

Simultaneous light and information–power transfer (SLIPT) offers a compelling strategy to overcome this limitation by enabling a single device to harvest optical energy while decoding high-speed data. In principle, perovskite solar cells are well suited to this role owing to their high open-circuit voltages, strong optical responsivity enabling photodiode-like operation[11]. Previous demonstrations have shown that perovskite devices can alternately support either efficient power extraction or high-speed data

transmission using the same optical source[12]. However, these functionalities have typically been realised under different operating conditions, and the impact of photovoltaic bias on communication performance has not been systematically examined.

This gap in understanding is critical. Operating a device near short circuit or near the MPP fundamentally alters the internal electric field, charge extraction pathways, interfacial recombination, and capacitive charging. These changes are expected to strongly influence the high-frequency response[13], yet the physical mechanisms governing communication bandwidth under photovoltaic operating conditions remain unresolved. To date, no study has established whether high-speed communication can be sustained during efficient power harvesting, nor how device design should be optimised to enable true SLIPT operation.

Here, we address this challenge by systematically engineering the hole-transport layer (HTL) in inverted PSCs to decouple photovoltaic efficiency from communication bandwidth. We compare representative HTLs spanning a wide range of interfacial energetics and conductivities, PEDOT: PSS, PTAA, and MeO-2PACz, and further tune charge extraction using molecular p-doping of PTAA with F4TCNQ. By operating all devices directly at their maximum power point, we perform a rigorous, like-for-like evaluation of power harvesting and data transmission under realistic SLIPT conditions. Combining high-speed optical communication experiments with transient photoluminescence, transient photocurrent measurements, and bias-dependent electrochemical impedance spectroscopy, we identify the physical mechanisms governing bandwidth under photovoltaic bias. We show that communication performance is not limited by carrier lifetime or interfacial recombination, but instead by the geometric RC response of the transport-layer stack. Importantly, we find that RC limitations are minimised near the maximum power point, enabling devices to retain a large fraction of their short-circuit data rate while simultaneously delivering useful electrical power.

These results establish fundamental design rules for high-speed, energy-harvesting perovskite receivers and demonstrate the feasibility of truly simultaneous visible-light communication and power extraction using inverted perovskite solar-cell architectures.

2. Results and Discussion

2.1. Energy-harvesting performance and implications for SLIPT

We first establish the photovoltaic performance of inverted perovskite solar cells incorporating different HTLs to define the baseline for SLIPT. Devices were characterised under AM1.5G illumination, indoor lighting (1000 lux, 0.3 mW cm^{-2}), and 650 nm laser excitation (13 mW cm^{-2}) representative of visible-light communication (VLC) sources. Figure 1a summarises the power-conversion efficiencies, and the full devices parameters are provided in **Table S1**. Consistent with interfacial energy-energy level alignment, devices employing MeO-2PACz self-assembled monolayer exhibit the highest photovoltaic

performance, approaching 20% under 1-sun. In contrast, PEDOT: PSS-based devices showed substantially lower open-circuit voltages (V_{OC}) and efficiencies (~ 12%) due to a pronounced HOMO-level mismatch with the perovskite absorber (Fig. 2a), This mismatch introduces interfacial band bending and reduces quasi-Fermi level splitting, thereby limiting V_{OC}[14].

Molecular p-doping of PTAA using F4TCNQ yields modest but reproducible performance improvements, reflecting enhanced hole conductivity and more favourable interfacial energetics[15, 16]. Under 650 nm laser illumination, all devices generated notably higher electrical power than under indoor lighting, owing to the strong spectral responsivity of the perovskite absorber at this wavelength[17] (Fig. 1b). Importantly, this enables efficient energy harvesting using the same optical carrier that encodes data. Although higher power could in principle be harvested close to the responsivity peak (~ 750 nm), 650 nm is chosen here to align with established VLC sources. The maximum electrical harvested powers under all illumination conditions are summarized in Table 1, revealing a clear hierarchy: MeO-2PACz delivers the highest power, PEDOT: PSS the lowest, with pristine and doped PTAA lying in between. This hierarchy raises a central question for SLIPT: does the HTL that maximises photovoltaic power simultaneously enable the highest communication bandwidth?

Table 1
Power harvested under different illumination conditions and summary of SNR-derived bandwidths and data rate closer to short-circuit condition.

HTL	AM1.5G	650nm Laser	Indoor Light	-3dB BW From SNR	-6dB Usable BW From SNR	Data Rate
	(mW)	(μW)	(μW)	(MHz)	(MHz)	(Mbps)
PEDOT: PSS	114.55	359.5	5.7	10.07	14.60	62.41
MeO-2PACz	175.40	631.7	8.3	5.23	11.48	45.79
PTAA	135.98	397.3	6.2	4.06	8.82	38.95
Doped PTAA	142.39	476.0	6.5	4.45	9.76	48.35

2.2. Communication performance near short-circuit current operation

We first assessed the communication characteristics of all devices under short-circuit conditions, which are typically optimal for photovoltaic receivers owing to strong photocurrent dynamics and minimal influence from internal field redistribution[18]. In optoelectronic devices such as photodiodes, the electrical − 3 dB bandwidth (f_{3dB}) defines the detector cut-off frequency and limits the maximum achievable data-transmission rate[17, 19]. To evaluate the intrinsic bandwidth under realistic communication conditions, we measured the signal-to-noise ratio (SNR) using a modulated optical link (Fig. 1c). The SNR as a function of frequency under short-circuit operation is shown in Fig. 1d. The

dotted line indicates the − 6 dB cut-off, which represents the performance-driven limit for practical communication. This range was used for data allocation data in the data rate measurements, and SNR-based metrics are employed in subsequent analyses for practical relevance[20]. The results show that devices based on PEDOT: PSS exhibit the largest − 6 dB bandwidth (~ 15MHz), whereas devices incorporating the other HTLs cluster around 10MHz (Table 1).

Using DC-biased optical orthogonal frequency division multiplexing (DCO-OFDM), we extracted maximum data rates at a bit error ratio (BER) of $3x10^{-3}$, a threshold considered sufficient to ensure reliable operation after forward error correction (FEC). As expected, the achievable data rates scale with both SNR and bandwidth. PEDOT: PSS-based devices achieve the highest data rates despite their inferior photovoltaic performance (Table 1). Notably, no monotonic correlation is observed between photovoltaic efficiency and communication speed: HTLs that maximise power extraction do not necessarily enable the highest bandwidth.

All devices employ the same perovskite absorber with comparable crystallinity, as confirmed by X-ray diffraction (**Figure S1**), making differences in trap-mediated recombination or carrier diffusion lengths unlikely to be the origin of the observed variations. Charge-transfer limitations at the electron-transport-layer (ETL) side can also be excluded, as all devices use an identical $PC_{60}BM$/BCP stack. The differences in communication performance must therefore originate from HTL-related factors, such as charge-extraction kinetics, interfacial recombination dynamics, or RC constraints imposed by the conductivity and capacitance of the hole transport layers. To identify the physical origin of these discrepancies, we next systematically investigate interfacial recombination, transient charge-extraction dynamics, and RC limitations.

2.3. Interfacial recombination and transient charge extraction

To probe interfacial recombination, we performed time-resolved photoluminescence (TRPL) measurements on perovskite films deposited on different HTLs (Fig. 2b). PEDOT: PSS yields the shortest average carrier lifetime, dominated by a fast decay component, consistent with its substantial energetic mismatch suppressing hole back-transfer into the perovskite (Fig. 2a). In contrast, MeO-2PACz exhibits a pronounced delayed decay component, indicating partial hole back-transfer enabled by closer energetic alignment. F4TCNQ-doped PTAA similarly shows an increased delayed recombination relative to pristine PTAA, confirming that improved energetics facilitate partial hole back-transfer in doped PTAA-based devices[21].

Despite these differences in interfacial dynamics, no monotonic correlation is observed between TRPL lifetime and communication bandwidth across the device set. Notably, MeO-2PACz-based devices exhibit long carrier lifetimes yet still support moderate communication speeds, indicating that interfacial recombination alone does not determine the high-frequency response.

Transient photocurrent (TPC) measurements provide further insight into charge-extraction dynamics across the full device stack[22] (Fig. 2c). The rising edge of the photocurrent exhibits two distinct features: a fast initial peak associated with the rapid extraction of interfacial charges accumulated in the dark, followed by a slower peak corresponding to steady-state extraction of photogenerated carriers once the junction reaches equilibrium [23]. PEDOT: PSS based devices display a pronounced initial current spike, attributed to rapid de-accumulation of interfacial charge accumulated in the dark due to energetic mismatch. This capacitive discharge enhances the initial transient response and contributes to improved high-frequency signal components. For MeO-2PACz, the separation between the two current peaks is minimal, indicating nearly simultaneous extraction of accumulated and photogenerated charges. HTL with intermediate energy-level alignment (i.e., PTAA) show correspondingly intermediate peak structures. However, all devices show similar falling-edge transients, indicating comparable recombination or extraction dynamics once illumination ceases. Since usable communication bandwidth depends on both rise and fall times[24], these results suggest that transient extraction alone cannot account for the measured bandwidth differences and global RC limitations may probably dominate the frequency response.

To directly probe resistive and capacitive constraints, we performed electrochemical impedance spectroscopy (EIS) under 650 nm illumination. At high frequencies, ionic motion is effectively frozen and the impedance response reflects purely electronic transport and capacitance[25]. The high-frequency semicircle in the Nyquist spectra (Fig. 2d) is well described by a parallel RC element dominated by the geometric capacitance of the device. PEDOT: PSS-based devices exhibit the lowest capacitance, while pristine PTAA shows the highest, with MeO-2PACz and doped PTAA lying in between. This trend closely mirrors the measured communication bandwidths. Because device area and absorber thickness are fixed, the capacitance variations arise primarily from HTL properties. Highly conductive HTLs reduce charge accumulation and effective capacitance, thereby lowering the RC time constant, while molecular p-doping further suppresses capacitance by enhancing hole conductivity[15]. Together, these results establish that communication bandwidth in perovskite solar cells is governed primarily by RC limitations rather than by carrier lifetime or interfacial recombination.

2.4. Simultaneous energy harvesting and communication at the maximum power point (MPP)

We finally evaluate device performance under true SLIPT conditions by operating all devices directly at their maximum power point using a bias-tee configuration that separates the AC (communication) and DC (power harvesting) components. Remarkably, all devices retain more than 70% of their short-circuit data rate at the MPP (Table 2), demonstrating that high-speed optical communication can be sustained during efficient power extraction.

Comparative SNR measurement at the MPP (Fig. 3a) show that PEDOT: PSS-based devices achieve an SNR of ~ 22.5 dB with a usable bandwidth of ~ 14.9 MHz, delivering the highest data rate (52.3 Mbps) but the lowest harvested power (~ 360μW). In contrast, F4TCNQ-doped PTAA achieves a more balanced

performance, delivering ~ 475 μW while sustaining a ~ 40 Mbps data rate with a usable bandwidth of 11.71MHz, while undoped PTAA yields ~ 33 Mbps data rate with a usable bandwidth of 10.07 MHz. Devices employing the MeO-2PACz yield the highest harvested power (~ 630 μW) but experience a larger reduction in bandwidth and data rate relative to short-circuit operation (Fig. 3a and 3b, Table 2).

Taken together, these results are counterintuitive. As the operating point shifts from short circuit toward open circuit, the internal electric field weakens and mobile ions redistribute within the perovskite and at selective interfaces, processes that are typically expected to degrade high-frequency response[10]. Instead, the observed reduction in data rate is modest and non-linear, indicating that additional compensating mechanisms are active near the MPP.

All devices were therefore evaluated across the full bias range, from short circuit to open circuit, by varying the load connected to the DC branch of the bias-tee tee **(**Fig. 1c: section highlighted in red**)**. A representative bias-dependent data-rate measurement for a PEDOT: PSS-based device is shown in **Figure S6**. For all devices, the highest communication performance was observed near the MPP, following the short-circuit condition.

To understand why high-speed performance persists at the MPP, we performed EIS across the full operating voltage range, from short circuit to open circuit. Similar to measurements near short-circuit, two dominant contributions are identified at the MPP: a high-frequency (HF) semicircle, characterised by R_{HF} and C_{HF}, which captures the intrinsic electronic response with mobile ions effectively frozen, and a low frequency (LF) contribution, described by R_{LF} and C_{LF}, associated with slower interfacial and ionic charge-transfer processes.

Table 2
Communication performance at short-circuit (SC) and maximum power point (MPP), including the data-rate retention metric (D_{MPP}/D_{SC}). Second section shows bandwidths calculated from EIS fitting parameters. Values in brackets correspond to uncorrected EIS-derived badwidths prior to application of the proportionality factor k.

Measured						**Calculated from the EIS analysis**		
Data Rate @ SC	**Data Rate @ MPP**	**Data Rate after aging @ MPP**	D_{MPP}/D_{SC}	**-6dB BW @ MPP**	**-3dB BW @ MPP**	$k \cdot R_S \cdot C_{HF}$	$R_{HF} \cdot C_{HF}$	
(Mbps)	**(Mbps)**	**(Mbps)**	**(%)**	**(MHz)**	**(MHz)**	**(MHz)**	**(MHz)**	
PEDOT: PSS	62.41	52.33	48.87	84	14.92	8.04	6.14(1.72)	0.28
MeO-2PACz	45.79	31.13	29.77	68	9.76	4.29	4.32(1.21)	0.12
PTAA	38.95	33.08	32.27	85	10.07	5.07	5.18(5.07)	0.14
PTAA: F4TCNQ	48.35	40.38	38.03	84	11.71	6.25	6.04(6.25)	0.04

As the applied bias increases from short circuit toward open circuit, the impedance spectra evolve systematically. Between the MPP and open circuit, the spectra are dominated by a single semicircle, as illustrated for PEDOT: PSS-based devices in Fig. 3d (full datasets are shown in **Figure S3**). Near V_{OC}, a weak additional feature (see zoomed inset, Fig. 3d) appears at very high frequencies (1–10 MHz) and progressively merges with the main HF arc as the bias shifts toward the MPP or lower voltages. This feature is attributed primarily to the geometric capacitance of the device; its disappearance indicates that the geometric capacitance becomes increasingly masked by dominant electronic processes under operating conditions[26]. Below the MPP, two positive semicircles corresponding to HF and LF processes are clearly resolved, both increasing in magnitude at lower voltages, while the semicircles near the MPP remain the smallest and most well-defined.

At low operating voltages, close to short-circuit, the strong electric field across the perovskite layer drives efficient charge extraction (Fig. 4a). In this regime, the response is dominated by electronic transport and recombination, giving rise to two well-defined positive semicircles associated with HF (electronic) and LF (interfacial/ionic) processes.

The impedance spectra were fitted using an equivalent circuit consisting of a series resistance (R_S) accounting for contacts and wiring, followed by two parallel RC branches in series **(Figure S2)**. The HF branch describes the purely electronic response, where R_{HF} reflects coupled transport and

recombination resistance and C_{HF} corresponds primarily to the geometric capacitance of the perovskite layer, influenced by interfacial charge accumulation. The LF branch accounts for slower interfacial and ionic processes. This two RC topology reliably reproduces the impedance features commonly observed in perovskite solar cells and photodiodes and enables separation of electronic and ionic contributions [27].

The radius of HF semicircle exhibits a pronounced U-shaped dependence on bias (Fig. 4b), reaching a minimum at the MPP and increasing at both lower and higher voltages. This behaviour indicates that the effective high-frequency resistance (R_{HF}) is limited by extraction inefficiencies at low bias and by interfacial charge accumulation near V_{OC} [28]. At the MPP, these limitations are minimised and HF response is governed predominately by recombination resistance. In contrast, C_{HF} remains approximately constant at low voltages, corresponding to the geometric capacitance of the device, and increases exponentially at higher voltages due to bulk and interfacial charge accumulation [29], [30]. Therefore, the RC limitation is weakest near the MPP. This effect compensates for the reduction in photocurrent response caused by the diminishing internal electric field as the operating point moves from short circuit toward open circuit. As a result, devices exhibit enhanced data rates near the MPP, as schematically summarised in **Fig. 4a**.

Figure 4

(a) Schematic representation of the dominant mechanisms at different operating points of the solar cell. Yellow arrows indicate the electric field across the device under short-circuit, MPP, and open-circuit conditions. The corresponding equivalent circuit models and representative EIS semicircles are shown below. (b) Bias dependence of R_{HF} *for devices with different HTLs. (c) Bias dependence of* C_{HF} *for devices with different HTLs.*

From HF branch, a characteristic electronic time constant can be defined as

$$\tau_{HF} = R_{HF} \cdot C_{HF}$$

With the associated characteristic frequency

$$f_{HF} = \frac{1}{2\pi \tau_{HF}}$$

For a single-pole RC-limited response, the bandwidth is given by

$$f_{3dB} = \frac{1}{2\pi R_{tot} C_{tot}}$$

where R_{tot} is the effective series resistance and C_{tot} is the total geometric capacitance.

To connect the impedance analysis with the measured optical bandwidths, we compare the experimentally determined f_{3dB} with characteristic frequencies extracted from the HF impedance

response using R_s, R_{HF}, C_{HF} evaluated at the MPP (Table 2). We acknowledge that a direct comparison between the electronic characteristic frequency obtained from impedance spectroscopy and the optically measured − 3 dB bandwidth is not strictly equivalent, as the two techniques probe the device under different excitation conditions and measurement configurations. Our objective, however, is to compare intrinsic device parameters governing the electrical response. To enable meaningful comparison, we introduce a proportionality constant, k, that accounts for the measurement transfer function of the potentiostat, including calibration factors and additional resistive contributions from the instrument and external wiring. This correction isolates the device-limited RC response from extrinsic measurement artefacts, allowing consistent comparison between impedance-derived frequencies and optically measured bandwidth.

$$f_{HF} = \frac{1}{2\pi\, R_S C_g k}$$

The measured − 3dB bandwidth correlate closely with the trend expected from $k.R_S.C_g$ (Table 2), where $k = 0.28$, C_g corresponds to the flat, low-bias region of C_{HF}, and R_S includes the series and interfacial transfer resistances from the perovskite absorber to the HTL. The PEDOT: PSS-based device exhibits a higher measured bandwidth, consistent with the capacitive interfacial behaviour discussed in the TPC analysis. Overall, this agreement demonstrates that the communication bandwidth is primarily limited by the external RC pathway rather than intrinsic recombination dynamics.

To assess operational stability, devices were operated under maximum power point tracking for 500 hours while monitoring their data rates. No significant degradation in communication performance was observed (Fig. 3b), and the encapsulation ensured stable photovoltaic efficiency throughout the measurement period (MPP tracking data in **Figure S7**). With continued improvements in perovskite device stability, this approach offers a promising route toward practical SLIPT-enabled optoelectronic systems for Internet-of-Things and indoor wireless applications.

3. Conclusion

This work demonstrates that perovskite solar cells can function as high-speed optical receivers while simultaneously harvesting electrical power at their maximum power point. Contrary to the prevailing assumption that optical communication in photovoltaic devices must be confined to short-circuit operation, we show that inverted perovskite devices retain a large fraction of their communication bandwidth and data rate under photovoltaic bias, even while extracting substantial electrical power. By systematically engineering the hole-transport layer through material selection and controlled molecular p-doping, we decouple photovoltaic efficiency from communication speed and identify the physical mechanisms governing SLIPT performance. Using complementary transient and impedance-based measurements, we demonstrate that communication bandwidth is not limited by carrier lifetime or interfacial recombination, but Instead by the geometric RC response of the transport-layer stack. RC limitations are minimal near the maximum power point, allowing data transmission during power

extraction, with the frequency response governed primarily by the circuit's series resistance, including HTL transfer resistance, and the device's geometric capacitance.

These findings establish clear design rules for simultaneous energy harvesting and optical communication: high-speed SLIPT requires minimising geometric capacitance and resistive losses in transport layers rather than maximising photovoltaic efficiency alone. More broadly, this work positions perovskite photovoltaics as a viable platform for self-powered visible-light communication, with implications for energy-autonomous sensors, indoor wireless networks, and integrated optoelectronic systems.

Declarations

Conflict of Interest

The authors declare no competing interests.

Author Contribution:

M.T.S. and H.M. conceived the research idea. M.T.S. secured funding for the project. H.M fabricated, optimised, and characterised the devices. H.M wrote the first draft of manuscript. M.A., B.B., and H.M. conducted the data communication experiments and M.A. performed the related analyses. A.J.R. performed the EIS analysis and assisted with data interpretation. H.L. and S.H. assisted with transient photocurrent measurements and stability tests. J. H. assisted with device fabrication. M.A., J.B., S.D., H.H., M.A.-J., I.T., and M.T.S. provided feedback and contributed to manuscript review and editing. M.A.-J., I.T., and M.T.S., supervised the project. All authors reviewed and approved the final manuscript.

Acknowledgement:

H.M, B.B., S.D., J.B., and M.T.S. are grateful to London South Bank University for financial support and PhD scholarship for H.M. and B.B. M.T.S., H.M., and B.B. also acknowledge financial support from EPSRC (UKRI647) and British Council (grant numbers F41). M.A.-J., S.H. and H.L. gratefully acknowledge the funding received from the European Union's Horizon Europe research and innovation program for the SUNPEROM project, Grant Agreement No. 101223212. M.A.-J., S.H. and H.L. acknowledges University College London's Research, Innovation and Global Engagement, UCL – Korea University Strategic Partner Fund for their financial support. M. A. is grateful for Engineering and Physical Sciences Research Council (EPSRC) grant EP/S022139/1 - the Centre for Doctoral Training in Connected Electronic and Photonic Systems. A.J.R. acknowledge the European Research Council (ERC) for funding (grant agreement number 832606; project PISCO).

Data availability

The data has been included in the supplementary information (SI). Supplementary information is available.

References

1. 'Best Research-Cell Efficiency Chart'. Accessed: Aug. 19, 2024. [Online]. Available: https://www.nrel.gov/pv/cell-efficiency.html
2. M. Helal Miah, M. Uddin Khandaker, M. Bulu Rahman, M. Nur-E-Alam, and M. Aminul Islam, 'Band gap tuning of perovskite solar cells for enhancing the efficiency and stability: issues and prospects', *RSC Adv.*, vol. 14, no. 23, pp. 15876–15906, 2024, doi: 10.1039/D4RA01640H.
3. S. D. Stranks *et al.*, 'Electron-Hole Diffusion Lengths Exceeding 1 Micrometer in an Organometal Trihalide Perovskite Absorber', *Science*, vol. 342, no. 6156, pp. 341–344, Oct. 2013, doi: 10.1126/science.1243982.
4. D. Meggiolaro *et al.*, 'Iodine chemistry determines the defect tolerance of lead-halide perovskites', *Energy Environ. Sci.*, vol. 11, no. 3, pp. 702–713, Mar. 2018, doi: 10.1039/C8EE00124C.
5. S. Srivastava *et al.*, 'Advanced spectroscopic techniques for characterizing defects in perovskite solar cells', *Commun. Mater.*, vol. 4, no. 1, Jul. 2023, doi: 10.1038/s43246-023-00379-y.
6. L. Min *et al.*, 'Frequency-selective perovskite photodetector for anti-interference optical communications', *Nat. Commun.*, vol. 15, no. 1, p. 2066, Mar. 2024, doi: 10.1038/s41467-024-46468-5.
7. L. Shen *et al.*, 'A Self-Powered, Sub-nanosecond-Response Solution-Processed Hybrid Perovskite Photodetector for Time-Resolved Photoluminescence-Lifetime Detection', *Adv. Mater.*, vol. 28, no. 48, pp. 10794–10800, 2016, doi: 10.1002/adma.201603573.
8. H. Zhu *et al.*, 'Solution-processed CsPbBr3 perovskite films via CsBr intercalated PbBr2 intermediate for high-performance photodetectors towards underwater wireless optical communication', *Nano Energy*, vol. 125, p. 109513, Jun. 2024, doi: 10.1016/j.nanoen.2024.109513.
9. J. G. Graeme, *Photodiode Amplifiers: OP AMP Solutions*. McGraw Hill Professional, 1996.
10. 'Basic Structure of Solar Cells', in *Physics of Solar Cells*, John Wiley & Sons, Ltd, 2005, pp. 109–136. doi: 10.1002/9783527618545.ch6.
11. J.-P. Correa-Baena *et al.*, 'The rapid evolution of highly efficient perovskite solar cells', *Energy Environ. Sci.*, vol. 10, no. 3, pp. 710–727, Mar. 2017, doi: 10.1039/C6EE03397K.
12. N. A. Mica *et al.*, 'Triple-cation perovskite solar cells for visible light communications', *Photonics Res.*, vol. 8, no. 8, p. A16, Aug. 2020, doi: 10.1364/PRJ.393647.
13. S. Donati, *Photodetectors: Devices, Circuits and Applications*. John Wiley & Sons, 2020.
14. M. Stolterfoht *et al.*, 'Approaching the fill factor Shockley–Queisser limit in stable, dopant-free triple cation perovskite solar cells', *Energy Environ. Sci.*, vol. 10, no. 6, pp. 1530–1539, Jun. 2017, doi:

10.1039/C7EE00899F.

15. Y. Zhang, M. Elawad, Z. Yu, X. Jiang, J. Lai, and L. Sun, 'Enhanced performance of perovskite solar cells with P3HT hole-transporting materials via molecular p-type doping', *RSC Adv.*, vol. 6, no. 110, pp. 108888–108895, Nov. 2016, doi: 10.1039/C6RA21775C.
16. G. Zhang, L. Yang, X. Wang, Z. Wu, J. Jiang, and Y. Luo, 'Energy Materials Design for Steering Charge Kinetics', *Adv. Mater.*, vol. 30, no. 48, p. 1801988, 2018, doi: 10.1002/adma.201801988.
17. L. Dou *et al.*, 'Solution-processed hybrid perovskite photodetectors with high detectivity', *Nat. Commun.*, vol. 5, no. 1, p. 5404, Nov. 2014, doi: 10.1038/ncomms6404.
18. S. Zhang *et al.*, 'Organic solar cells as high-speed data detectors for visible light communication', *Optica*, vol. 2, no. 7, pp. 607–610, Jul. 2015, doi: 10.1364/OPTICA.2.000607.
19. Y. Xu and Q. Lin, 'Photodetectors based on solution-processable semiconductors: Recent advances and perspectives', *Appl. Phys. Rev.*, vol. 7, no. 1, p. 011315, Mar. 2020, doi: 10.1063/1.5144840.
20. J. M. Kahn and J. R. Barry, 'Wireless Infrared Communications'.
21. J. E. Lee *et al.*, 'Unraveling Loss Mechanisms Arising from Energy-Level Misalignment between Metal Halide Perovskites and Hole Transport Layers', *Adv. Funct. Mater.*, vol. 34, no. 30, p. 2401052, 2024, doi: 10.1002/adfm.202401052.
22. B. C. O'Regan, P. R. F. Barnes, X. Li, C. Law, E. Palomares, and J. M. Marin-Beloqui, 'Optoelectronic Studies of Methylammonium Lead Iodide Perovskite Solar Cells with Mesoporous TiO2: Separation of Electronic and Chemical Charge Storage, Understanding Two Recombination Lifetimes, and the Evolution of Band Offsets during J–V Hysteresis', *J. Am. Chem. Soc.*, vol. 137, no. 15, pp. 5087–5099, Apr. 2015, doi: 10.1021/jacs.5b00761.
23. M. De Bastiani *et al.*, 'Interfacial Dynamics and Contact Passivation in Perovskite Solar Cells', *Adv. Electron. Mater.*, vol. 5, no. 1, p. 1800500, 2019, doi: 10.1002/aelm.201800500.
24. K. Hu *et al.*, 'Binary response Se/ZnO p-n heterojunction UV photodetector with high on/off ratio and fast speed', *Laser Photonics Rev.*, vol. 11, no. 1, p. 1600257, 2017, doi: 10.1002/lpor.201600257.
25. W. Tress, 'Metal Halide Perovskites as Mixed Electronic–Ionic Conductors: Challenges and Opportunities—From Hysteresis to Memristivity', *J. Phys. Chem. Lett.*, vol. 8, no. 13, pp. 3106–3114, Jul. 2017, doi: 10.1021/acs.jpclett.7b00975.
26. E. Von Hauff and D. Klotz, 'Impedance spectroscopy for perovskite solar cells: characterisation, analysis, and diagnosis', *J. Mater. Chem. C*, vol. 10, no. 2, pp. 742–761, 2022, doi: 10.1039/D1TC04727B.
27. A. J. Riquelme, K. Valadez-Villalobos, P. P. Boix, G. Oskam, I. Mora-Seró, and J. A. Anta, 'Understanding equivalent circuits in perovskite solar cells. Insights from drift-diffusion simulation', *Phys. Chem. Chem. Phys.*, vol. 24, no. 26, pp. 15657–15671, 2022, doi: 10.1039/D2CP01338J.
28. S. Shao and M. A. Loi, 'The Role of the Interfaces in Perovskite Solar Cells', *Adv. Mater. Interfaces*, vol. 7, no. 1, p. 1901469, 2020, doi: 10.1002/admi.201901469.

29. A. Riquelme *et al.*, 'Identification of recombination losses and charge collection efficiency in a perovskite solar cell by comparing impedance response to a drift-diffusion model', *Nanoscale*, vol. 12, no. 33, pp. 17385–17398, 2020, doi: 10.1039/D0NR03058A.

30. D. Kiermasch, A. Baumann, M. Fischer, V. Dyakonov, and K. Tvingstedt, 'Revisiting lifetimes from transient electrical characterization of thin film solar cells; a capacitive concern evaluated for silicon, organic and perovskite devices', *Energy Environ. Sci.*, vol. 11, no. 3, pp. 629–640, Mar. 2018, doi: 10.1039/C7EE03155F.

Figures

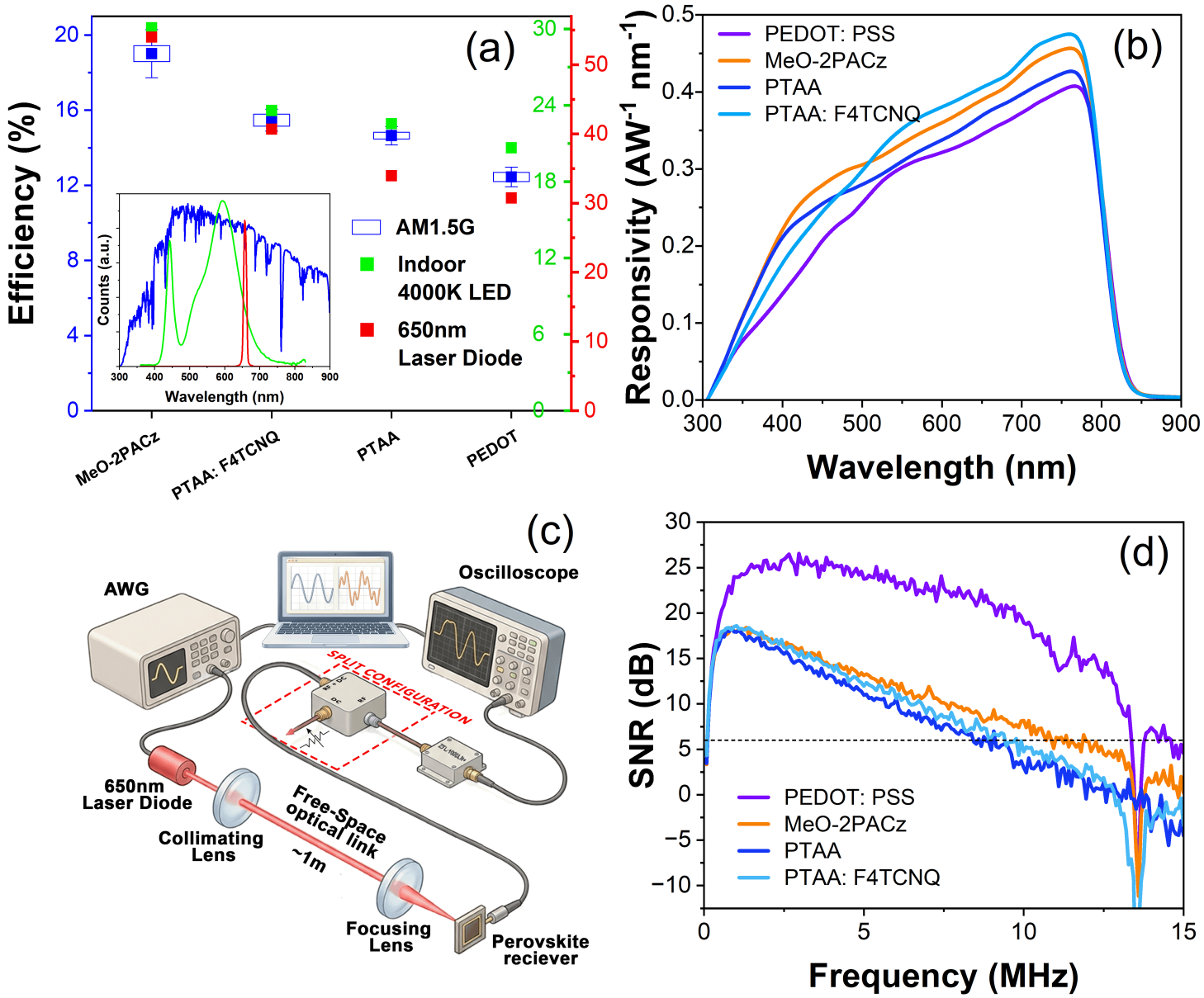


Figure 1

(a) Distribution of the PCE under different illumination sources, relevant spectra are shown in the inset. (b) Spectral responsivity of devices with different HTLs. (c) Schematic illustration of the optical communication link used for measurements, (d) SNR plots of devices with different HTLs close to the short-circuit conditions.

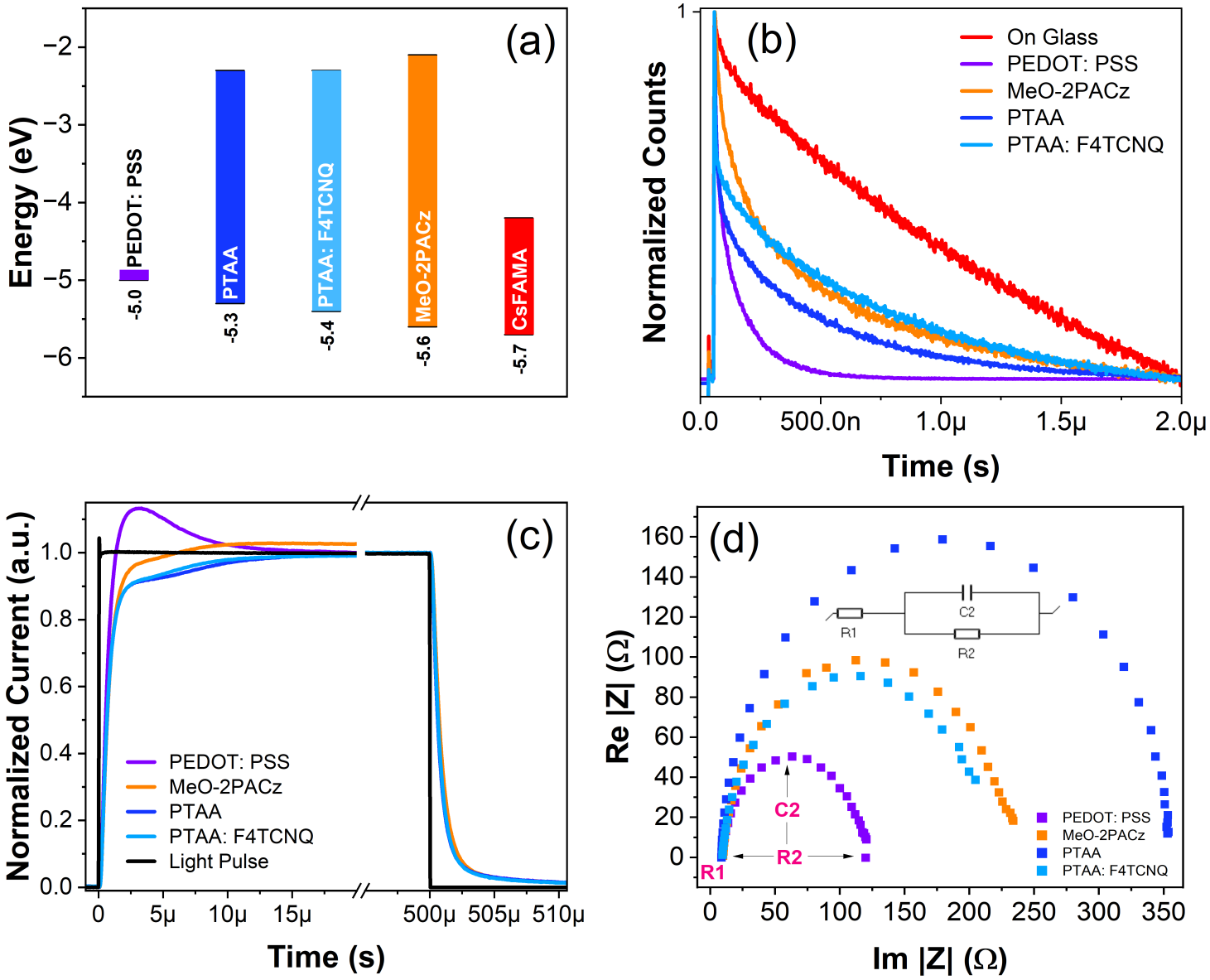


Figure 2

(a) Energy-level alignment of the HTLs with the Perovskite absorber. (b) Time-resolved photoluminescence (TRPL) decay of the perovskite films on different HTLs. (c) Transient photocurrent (TPC) response of devices with different HTLs. (d) High-frequency semicircle of the EIS spectra near short-circuit operation.

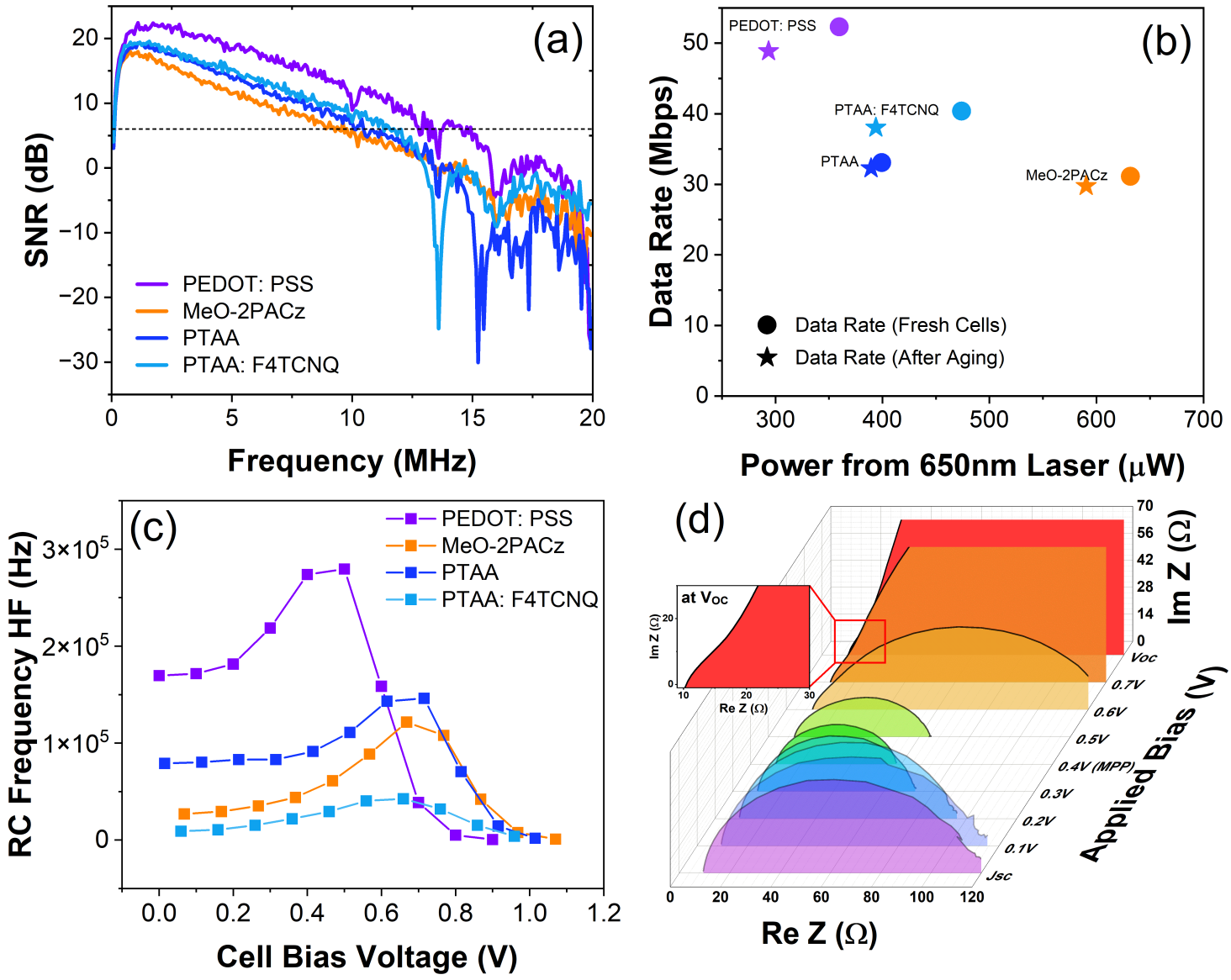


Figure 3

(a) SNR spectra measured at the maximum power point (MPP). (b) Comparison of data rates vs. harvested power for different HTLs. (c) Characteristic RC frequencies extracted from EIS fitting. (d) Evolution of the high-frequency semicircle in EIS spectra at different operational voltages (representative PEDOT: PSS device).

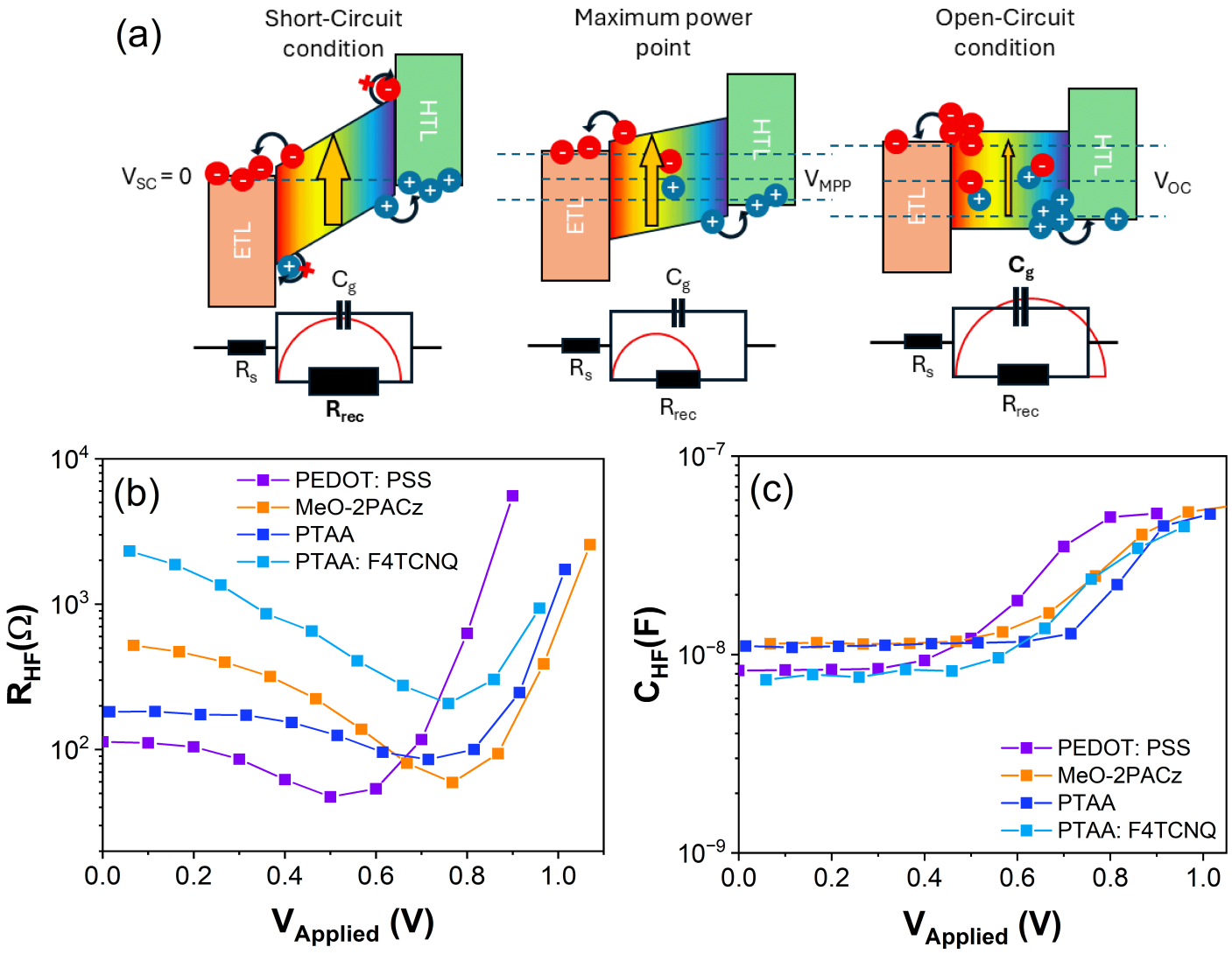


Figure 4

(a) Schematic representation of the dominant mechanisms at different operating points of the solar cell. Yellow arrows indicate the electric field across the device under short-circuit, MPP, and open-circuit conditions. The corresponding equivalent circuit models and representative EIS semicircles are shown below. (b) Bias dependence of F_{HF} for devices with different HTLs. (c) Bias dependence of C_{HF} for devices with different HTLs.

Supplementary Files

This is a list of supplementary files associated with this preprint. Click to download.

- SLIPTreceiversSI.docx